

**Speciated atmospheric mercury at Waliguan Global Atmospheric Watch station  
in the northeastern Tibetan Plateau: implication of dust related sources for  
particulate bound mercury**

Hui Zhang<sup>1</sup>, Xuewu Fu<sup>1,2\*</sup>, Ben Yu<sup>3</sup>, Baoxin Li<sup>4</sup>, Peng Liu<sup>4</sup>, Guoqing Zhang<sup>4</sup>, Leiming Zhang<sup>5</sup>,  
Xinbin Feng<sup>1,2,6\*</sup>

<sup>1</sup> State Key Laboratory of Environmental Geochemistry, Institute of Geochemistry, Chinese Academy of Sciences,  
99 Lincheng West Road, Guiyang, 550081, China.

<sup>2</sup> CAS Center for Excellence in Quaternary Science and Global Change, Xi'an, 710061, China.

<sup>3</sup> State Key Laboratory of Environmental Chemistry and Ecotoxicology, Research Center for Eco-Environmental  
Sciences, Chinese Academy of Sciences, Beijing, 100085, China.

<sup>4</sup> China Global Atmosphere Watch Baseline Observatory, Qinghai Meteorological Bureau, Xining, 810001, China.

<sup>5</sup> Air Quality Research Division, Science and Technology Branch, Environment and Climate Change Canada,  
Toronto, M3H5T4, Canada

<sup>6</sup> University of Chinese Academy of Sciences, Beijing, 100049, China.

Corresponding authors:

Xuewu Fu ([fuxuewu@mail.gyig.ac.cn](mailto:fuxuewu@mail.gyig.ac.cn)), Xinbin Feng ([fengxinbin@vip.skleg.cn](mailto:fengxinbin@vip.skleg.cn))

## 1 **Abstract**

2 To understand the ambient levels and sources of atmospheric mercury (Hg) in the Tibetan  
3 Plateau, a full-year continuous measurement of speciated atmospheric mercury was conducted at  
4 Waliguan (WLG) Baseline Observatory (3816 m a.s.l.) from May 2012 to April 2013. Mean  
5 concentrations ( $\pm 1SD$ ) of gaseous elemental mercury (GEM), gaseous oxidized mercury (GOM)  
6 and particulate bound mercury (PBM) during the whole study period were  $1.90 \pm 0.80 \text{ ng m}^{-3}$ ,  $12.0$   
7  $\pm 10.6 \text{ pg m}^{-3}$  and  $65.4 \pm 63.2 \text{ pg m}^{-3}$ , respectively. Seasonal variations of GEM were very small,  
8 while those of PBM were quite large with mean values being four times higher in cold ( $102.3 \pm 66.7$   
9  $\text{pg m}^{-3}$ ) than warm ( $22.8 \pm 14.6 \text{ pg m}^{-3}$ ) season. Anthropogenic emissions to the east of Tibetan  
10 Plateau contributed significantly to GEM pollution at WLG, while dust particles originated from  
11 desert and Gobi regions in Xinjiang province and Tibetan Plateau to the west of WLG were  
12 responsible to PBM pollution at WLG. This finding is also supported by the significant positive  
13 correlation between daily PBM concentration and daily cumulative absorbing aerosol index (AAI)  
14 encountered by air masses transported during the preceding two days.

15  
16 **Keywords:** Speciated atmospheric mercury, Particulate bound mercury, Anthropogenic mercury  
17 emissions, Dust related sources

## 18 19 **Introduction**

20 Mercury (Hg) is a toxic pollutant of global concern due to its long lifetime in air,  
21 bioaccumulation in aquatic system, and detrimental impacts on human and animal health.  
22 Atmospheric Hg is operationally defined in three forms, i.e., gaseous elemental mercury (GEM),  
23 gaseous oxidized mercury (GOM), and particulate bound mercury (PBM). These Hg species can be  
24 transformed among each other through complex physical and chemical processes (Lyman et al.,  
25 2020; Selin, 2009). For example, GEM can be oxidized to form GOM, and GEM and/or GOM can  
26 adsorb on atmospheric aerosols to form PBM (Ariya et al., 2015). GEM has a lifetime in air of 0.5-  
27 2 years while GOM and PBM only have a lifetime of hours to weeks (Ariya et al., 2015; Murphy et  
28 al., 2006). Because of their different lifetimes, GEM can be transported globally via atmospheric  
29 circulation whereas PBM is limited to regional transport (Pirrone et al., 2010). These Hg species  
30 can be removed from the atmospheric through dry and wet deposition processes. Once deposited to  
31 earth's surface, Hg can be converted to methylmercury by biological processes, which can cause  
32 potential risks to ecological and human health (Jonsson et al., 2014; Wright et al., 2018). On the  
33 other hand, Hg accumulated in soil and water bodies can be emitted into the atmosphere, which  
34 plays an important role in the global atmospheric Hg cycle (Obrist et al., 2018; Wang et al., 2016).

36       Spatiotemporal variations of atmospheric Hg and Hg speciation fractions within the total Hg  
37 are controlled by many factors, among which anthropogenic emissions are important ones (Driscoll  
38 et al., 2013; Fu et al., 2012b). Global anthropogenic Hg emissions to the atmosphere were estimated  
39 to be 2224 Mg yr<sup>-1</sup>, of which 82-87%, 10-18% and 3-4% were in the form of GEM, GOM and PBM,  
40 respectively (AMAP/UNEP 2018). In China, concentrations of GEM and PBM were generally  
41 elevated compare to the observations in Europe and America. The fractions of PBM in total  
42 atmospheric Hg in urban areas of China were in the range of 5.2–17.2%, higher than those from  
43 total anthropogenic Hg emissions (Fu et al., 2015; Zhang et al., 2015b). In addition, observations of  
44 speciated atmospheric Hg in China in both urban and rural areas of China showed generally higher  
45 PBM than GOM levels (Fu et al., 2015b), which is in contrast with the higher GOM than PBM  
46 fractions in the total anthropogenic Hg emissions in China (Zhang et al., 2015b). These findings  
47 indicate that additional emission sources and other physical and chemical processes contributed to  
48 the elevated PBM concentrations in China. For example, natural sources, such as biomass burning  
49 and dust related sources, and gas-particle partitioning can also produce PBM (Amos et al., 2012;  
50 Obrist et al., 2008). The impact of these sources and processes on atmospheric PBM, although is  
51 potentially important, has not been well investigated by previous studies.

52

53       Speciated atmospheric Hg has been monitored in China in recent years, but observations in the  
54 Tibetan Plateau region are very limited. The Tibetan Plateau, also known as the third pole of the  
55 world with an average altitude of over 4000 m a.s.l., is an ideal place for assessing transport and  
56 transformation of atmospheric pollutants in China and other Asian regions (Chen et al., 2019;  
57 Loewen et al., 2007). The Tibetan Plateau is surrounded by East Asia and South Asia, which are the  
58 two most important source regions of atmospheric Hg in the world (Zhao et al., 2013). The  
59 Taklamakan and Gobi deserts are located to the west and north, respectively, of the Tibetan Plateau.  
60 Since the Tibetan Plateau region is strongly impacted by westerlies, Indian Summer Monsoon and  
61 East Asia Summer Monsoon (Fig. 1), it is affected by air pollutants from anthropogenic and natural  
62 source regions adjacent to the Tibetan Plateau (Che et al., 2011). Previous studies postulated that air  
63 masses passing over the urban and industrial areas in western China and South Asia were important  
64 sources of atmospheric GEM at Waliguan and Nam Co (4730 m a.s.l.) on the northeastern edge and  
65 Midlands of the Tibetan Plateau, respectively (Fu et al., 2012a; Yin et al., 2018). At Shangri-La,  
66 located on the southeastern edge of the Tibetan Plateau, the identified atmospheric GEM source  
67 regions were also located in Southeast Asia and mainland China (Zhang et al., 2015a). Speciated  
68 atmospheric Hg measurement was only carried out during a warm season in Qomolangma Natural  
69 Nature Preserve (4276 m a.s.l.) of Tibetan Plateau (Lin et al., 2019). Low GEM concentrations  
70 (means: 1.33 to 1.42 ng m<sup>-3</sup>), but elevated PBM concentrations (means: 25.6 to 49.0 pg m<sup>-3</sup>), were

71 observed in middle and southern Tibetan Plateau as compared to those in rural central and eastern  
72 China (Yin et al., 2018; Lin et al., 2019). To date, long-term observations of speciated atmospheric  
73 Hg in the Tibetan Plateau region are still lacking, limiting our capacity to fully understand the  
74 spatiotemporal patterns of Hg in this region and associated source regions and controlling factors.

75

76 In this study, one-year continuous monitoring of speciated atmospheric Hg was carried out at  
77 WLG in Tibetan Plateau region. Data were analyzed carefully for exploring the ambient levels,  
78 seasonal and diurnal patterns, and source regions of speciated atmospheric Hg in this region.  
79 Knowledge generated from this study is needed for establishing future emission control policies in  
80 order to preserve many sensitive ecosystems in this region.

81

## 82 **2 Materials and methods**

### 83 **2.1 Measurement site**

84 The measurement site is situated at the summit of Mt. Waliguan located at northeastern edge  
85 of the Tibetan Plateau in northwest China. It is a station known as Waliguan (WLG) Baseline  
86 Observatory (100°54' E, 36°17' N, 3816 m a.s.l.) (Fig.1), which is the only station in inner Asia in  
87 the Global Atmospheric Watch (GAW) program of World Meteorological Organization (WMO).  
88 This area has a typical high plateau continental climate, and western winds dominant at the site (Fu  
89 et al., 2012a; Okamoto and Tanimoto, 2016; Xu et al., 2018). WLG is mainly surrounded by the arid  
90 and semi-arid grassland and desert lands. The population density is very low and industrial activities  
91 sparsely distributed within 80 km around WLG. Anthropogenic Hg emissions in Qinghai province  
92 is relatively low, and are mostly located to the east of WLG (Fu et al., 2015; Sun et al., 2020; Wu  
93 et al., 2006). The Taklimakan Desert and Gobi Desert of Xinjiang province are located to the west  
94 of WLG, and the Gobi Desert of Hexi Corridor and southern Inner Mongolia are located to the north  
95 of WLG (Fig. 1).

96

### 97 **2.2 Sampling method**

#### 98 **2.2.1 Measurements of speciated atmospheric mercury**

99 High-temporal resolution measurements of GEM, GOM and PBM were carried out using the  
100 2537B-1130-1135 Atmosphere Speciation Mercury Analysis System (Fig. 1, Tekran Inc., Toronto,  
101 Canada) from May 2012 to April 2013. The Tekran Model 2537B Mercury Vapour Analyzer  
102 provides continuous analysis of GEM in air at 0.1 ng m<sup>-3</sup> detection limit. The instrument samples  
103 air and captures vapour phase Hg on the cartridges containing ultra-pure gold adsorbent media. The  
104 amalgamated Hg is thermally desorbed and detected using Cold Vapour Atomic Fluorescence  
105 Spectrometry (CVAFS). The Model 1135 Particulate Mercury Unit, together with the Model 1130

106 Mercury Speciation Unit, allows the Model 2537B Mercury Vapor Analyzer to simultaneously  
107 monitor and differentiate between GEM, GOM and PBM (fine fraction, < 2.5  $\mu\text{m}$ ) in ambient air.  
108 KCl-coated annular denuders was installed in the specially designated location of Model 1130  
109 Mercury Speciation Unit before the instrument starts running. The typical detection limits for the  
110 GOM and PBM measurements during a 2-hour sampling duration are 2  $\text{pg m}^{-3}$ , respectively  
111 (<http://www.tekran.com/files/Tekran-2537B-Unique-Features.r103.pdf>). The instrument's  
112 workflow is controlled by the controller which is capable of executing an automatic sampling and  
113 analysis program (Fu et al., 2016; Lindberg et al., 2002). Due to the low air pressure at WLG, the  
114 total sampling flow rate of the GOM and PBM was programmed to be 6.6 lpm (referenced to  
115 standard temperature and pressure conditions). The Tekran 2537 was sampling GEM at a flow  
116 rate of 0.6 lpm, while the Tekran 1130 pump module pulled additional air at 6 lpm. A 2-hour  
117 duration was selected for GOM and PBM sampling, during which GEM is continuously  
118 measured at a 5-minute interval.

119 This system has been used to monitor atmospheric Hg species worldwide, including the North  
120 America Atmospheric Mercury Network (AMNet) and the Global Mercury Observation System  
121 (GMOS) (Lan et al., 2012; Sprovieri et al., 2016). In this study, data QA/QC procedure followed  
122 the GMOS Standard Operation Procedure and Data Quality Management (D'Amore et al., 2015).  
123 Although KCl-coated annular denuders have been the most popular and widely applied method for  
124 measuring ambient GOM, large analytical uncertainties in GOM may exist due to the trace level  
125 and complicated chemical compounds of GOM which may not be fully collected by denuders (Ariya  
126 et al., 2015; Cheng and Zhang, 2017; Gustin et al., 2015; Gustin et al., 2019). Analysis and  
127 discussions presented in this study are mostly focused on GEM and PBM, considering the larger  
128 uncertainties in GOM than GEM and PBM.

129

### 130 **2.2.2 Meteorological data and backward trajectory calculation**

131 Meteorological parameters, including air temperature (AT), relative humidity (RH), rainfall  
132 (RF), wind direction (WD) and wind speed (WS) were obtained from the local weather station at  
133 WLG. In order to identify the effect of long-range transport of Hg emissions on the distributions of  
134 atmospheric Hg at WLG, backward trajectories arriving the site at 100 m above the ground were  
135 calculated every 4 hours using the TrajStat software and gridded meteorological data from the Air  
136 Resource Laboratory, National Oceanic and Atmospheric Administration (NOAA) (Wang et al.,  
137 2009). To investigate the source regions potentially influencing GEM and PBM concentrations at  
138 WLG, a weighing algorithm based on measured concentrations, known as the concentration  
139 weighted trajectory (CWT) approach, was applied in this study. In this procedure, the CWT value  
140 indicates the source strength of a  $0.5^\circ \times 0.5^\circ$  grid cell ( $\text{CWT}_{ij}$ ) to the WLG and is defined as:

141 
$$C_{ij} = \frac{1}{\sum_{l=1}^M \tau_{ijl}} \sum_{l=1}^M C_l \tau_{ijl}$$

142 where  $C_{ij}$  is the average CWT value of speciated atmospheric Hg in the grid cell  $(i,j)$ ,  $C_l$  is the 4-h  
 143 means of measured Hg concentration at WLG,  $\tau_{ijl}$  is the number of trajectory endpoints in the grid  
 144 cell  $(i,j)$  associated with the  $C_l$  sample, and  $M$  is the number of samples that have trajectory endpoints  
 145 in grid cell  $(i,j)$ . A point filter is applied as the final step of CWT to eliminate grid cells with few  
 146 endpoints. Weighted concentration fields show concentration gradients across potential sources.  
 147 This method helps determine the relative significance of potential source regions (Cheng et al., 2013;  
 148 Zhang et al., 2016).

149

### 150 **2.2.3 Ancillary parameters and analysis**

151 Anthropogenic emissions of GEM and PBM in  $0.5^\circ \times 0.5^\circ$  grid cells in the studied domain  
 152 were obtained from the 2010 global emission dataset developed by the Arctic Monitoring and  
 153 Assessment program (AMAP) (AMAP/UNEP, 2013). Gridded monthly biomass burned areas at  
 154  $0.25^\circ$  spatial resolution were obtained from the fourth version of the Global Fire Emission Database  
 155 (GFED4) (Giglio et al., 2013). Absorbing Aerosol Index (AAI) constitutes one of the most useful  
 156 space-borne data sets, offering temporal and spatial information on UV absorbing aerosols (black  
 157 carbon, desert dust) distributions. Desert dust and biomass burning related aerosols are the dominant  
 158 aerosol types detected by the AAI, and AAI is therefore a useful parameter for qualitatively  
 159 identifying the dust and biomass burning related sources. The AAI data are available on daily and  
 160 monthly basis at a spatial resolution of  $1 \times 1$  degree. Generally, non-absorbing aerosols (e.g., sulfate  
 161 and sea-salt) yield negative AAI values, UV-absorbing aerosols (e.g., dust and smoke) yield positive  
 162 AAI values, and clouds yield near-zero values (Prospero et al., 2002). Such information can be used  
 163 for identifying distinct desert dust aerosol sources and analyzing dust and smoke transport patterns  
 164 (Chiapello et al., 1999; Kubilay et al., 2005; Moulin and Chiapello, 2004). A detailed description of  
 165 the AAI product is given in (Herman et al., 1997; Torres et al., 1998). In this study, Global monthly  
 166 gridded ( $1 \times 1$  degrees) AAI products during our study period were obtained from the Tropospheric  
 167 Emission Monitoring Internet Service (TEMIS) (<http://www.temis.nl/airpollution/absaai/>).

168

169 To study the effect of dust related sources on the variations in PBM concentration at WLG, we  
 170 calculated the daily cumulative AAI ( $\Sigma$ AAI) based on the 2-day backward trajectory and gridded  
 171 AAI data. Further analysis between the daily  $\Sigma$ AAI and mean PBM concentration were conducted  
 172 to assess the effect of dust related sources on the variations of PBM at WLG.

173

## 174 **3 Results and discussion**

### 175 **3.1 Concentrations of GEM, GOM and PBM**

176 Time series of hourly speciated atmospheric Hg concentrations is shown in Fig. 2. Mean  $\pm$  1sd  
177 (median) concentrations of GEM, GOM and PBM at WLG during the whole sampling campaign  
178 were  $1.90 \pm 0.80$  (1.59)  $\text{ng m}^{-3}$ ,  $12.0 \pm 10.6$  (8.6)  $\text{pg m}^{-3}$  and  $65.4 \pm 63.2$  (39.9)  $\text{pg m}^{-3}$ , respectively.  
179 Mean GEM level at WLG was relatively higher than the background levels in the Northern  
180 Hemisphere (1.5-1.7  $\text{ng m}^{-3}$ ) (Fu et al., 2015; Sprovieri et al., 2016). Mean GEM concentration at  
181 WLG was relatively lower than that early observed in Mt. Gongga (mean =  $3.98 \pm 1.62$   $\text{ng m}^{-3}$ , 1sd)  
182 and Shangri-La (mean =  $2.55 \pm 0.73$   $\text{ng m}^{-3}$ , 1sd) located on the eastern edge of the Tibetan Plateau  
183 in 2005 and 2009 respectively, but much higher than that later observed in Qomolangma Natural  
184 Nature Preserve (mean =  $1.42 \pm 0.37$   $\text{ng m}^{-3}$ , 1sd) and Nam Co (mean =  $1.33 \pm 0.24$   $\text{ng m}^{-3}$ , 1sd) in  
185 the inland Tibetan Plateau in 2016 and 2014 respectively (Fu et al., 2012b; Fu et al., 2009; Lin et  
186 al., 2019; Yin et al., 2018; Zhang et al., 2015a). In general, atmospheric GEM levels in remote areas  
187 are closely related to the regional atmospheric Hg budget. The inland Tibetan Plateau is sparsely  
188 populated and with no large-scale industrial activities. However, Some monitoring sites on the  
189 northeastern and eastern edges of the Tibetan Plateau, such as WLG, Mt. Gongga and Shangri-La,  
190 are not too far away from the anthropogenic Hg source regions in middle and eastern China, and  
191 thus were impacted by anthropogenic Hg emissions through long-range transport, which explained  
192 the relatively higher GEM concentrations at these stations than inland Tibetan Plateau stations (Fu  
193 et al., 2008; Zhang et al., 2015a). The impact of regional and long-range transport of Hg originated  
194 from anthropogenic emissions on the elevated GEM level at WLG will be discussed in details in  
195 section 3.2 and 3.3 below.

196

197 Currently, there is a great debate on the measurement accuracy of GOM using KCl-coated  
198 denuder, and a small load of Hg could also cause analytical uncertainties in Tekran-based GOM and  
199 PBM measurements (Ambrose, 2017). Therefore, GOM data in this study was only compared with  
200 previously reported data collected using the same method. The mean GOM concentration at WLG  
201 was slightly higher than those in rural areas of North America and China, but lower than those in  
202 urban areas in China (Fu et al., 2012b; Zhang et al., 2016). GOM is mainly affected by local to  
203 regional emission sources and atmospheric processes (Sheu and Mason, 2001). Since WLG is  
204 isolated from primary anthropogenic sources, the relatively high level of GOM at WLG was  
205 probably mainly caused by atmospheric processes. Intrusion of GOM enriched air from free  
206 troposphere could be one reason, a phenomenon that has been reported in Qomolangma Natural  
207 Nature Preserve in the southern Tibetan Plateau (Lin et al., 2019). Additionally, GOM at WLG  
208 generally showed relatively higher concentrations during daytime (Fig. S4), indicating in situ  
209 photochemical production of GOM as another important mechanism causing high GOM levels at

210 WLG.

211

212 PBM concentrations at WLG showed large variations with the maximum hourly value reaching  
213  $655 \text{ pg m}^{-3}$ . The overall mean PBM concentration at WLG ( $68.1 \text{ pg m}^{-3}$ ) was significantly higher  
214 (by up to  $\sim 5$ -40 times) than those reported for remote areas in the northern Hemisphere (Kim et al.,  
215 2012; Lan et al., 2012), but was similar to observations in the urban areas in China (Fu et al., 2012b;  
216 Fu et al., 2015). Elevated PBM concentrations in Chinese urban areas were most likely caused by  
217 strong local anthropogenic emissions. However, in the remote areas with few primary anthropogenic  
218 emissions, long-range transport should be the major cause for highly elevated PBM concentrations.  
219 PBM has an atmospheric residence time ranging from a few days to weeks and can undergo regional  
220 transport (Seigneur et al., 2004; Zhang et al., 2019). Therefore, high PBM levels at WLG were  
221 probably mainly caused by long-range transport of anthropogenic and natural emissions, which was  
222 discussed in details in the following Sections.

223

### 224 **3.2 Seasonal and diurnal distributions of GEM, GOM and PBM**

225 Daily values of GEM, GOM, PBM, AT, RH, WS, RF, and air water content were aggregated  
226 into monthly average values to reveal seasonal variations during the study period (Table S1 and Fig.  
227 3). In the discussion below, warm (May to October) and cold (November to April) seasons were  
228 compared. Mean GEM level in the cold season ( $1.84 \text{ ng m}^{-3}$ ) was relatively lower than that in the  
229 warm season ( $1.95 \text{ ng m}^{-3}$ ) (Table S1), which was likely due to the strengthening westerlies  
230 originated from or passing over regions with low anthropogenic emissions during the cold season  
231 (Zhang et al., 2015b). However, elevated monthly mean GEM levels were observed from February  
232 to April (Table S1, Fig. S1, Fig. S2), and many high GEM events were frequently observed in the  
233 cold season (Fig. S3), likely due to the long-range transport from northern South Asia where has  
234 been experiencing industrialization and urbanization and thus strong anthropogenic Hg emissions  
235 (AMAP/UNEP, 2018; Chakraborty et al., 2013). Airflows originated from these areas had high  
236 GEM concentrations and could be transported to WLG in the cold season (Lin et al., 2019; Yin et  
237 al., 2018). In addition, higher than seasonal-average GEM concentrations were also observed during  
238 July to September (Table S1, Fig. 3), which could be attributed to the strengthening East Asia  
239 Summer Monsoon during the warm season. The prevailing wind from the east direction (Fig. 4,  
240 Table S1) could transport GEM from eastern Qinghai and southern Gansu province of China to  
241 WLG during the East Asian Summer Monsoon season.

242

243 Unlike GEM, mean and median GOM and PBM values were both higher in the cold season  
244 than in the warm season (Table S1, Fig. 3, Fig. S1, Fig. S2). Also, the high GOM and PBM events

245 occurred mainly in the cold months (Fig. S3). Lower GOM and PBM concentrations in the warm  
246 season were probably attributed to the increasing removal processes of these water soluble Hg  
247 species, and this is consistent with previous observations with wet Hg deposition fluxes peaked in  
248 the warm rainy season (Cole et al., 2014). In addition, low RH in the cold season would be  
249 conducive to the formation of GOM and PBM through atmospheric chemical and physical  
250 transformations (Fain et al., 2009; Lin et al., 2019). Higher PBM concentrations at WLG were  
251 frequently detected with westerly and northerly winds (Fig. 4), which were mainly from the desert  
252 and Gobi areas of western Tibetan Plateau, Xinjiang, southern Gansu and southwestern Inner  
253 magnolia, suggesting that desert dust related sources in these regions could be potential sources of  
254 PBM at WLG in the cold season.

255

256 No significant differences in GEM concentration were observed between daytime (7:00-19:00,  
257  $1.89 \pm 1.01 \text{ ng m}^{-3}$ ) and nighttime (20:00-06:00,  $1.86 \pm 0.91 \text{ ng m}^{-3}$ ) at WLG (Fig. S4). This was  
258 also the case for PBM ( $80.0 \pm 81.5 \text{ pg m}^{-3}$  versus  $75.0 \pm 72.5 \text{ pg m}^{-3}$ ). The diurnal pattern of PBM at  
259 WLG was different from those observed in Nam Co, Qomolangma Natural Nature Preserve and Mt.  
260 Gongga in the Tibetan Plateau where PBM generally peaked during daytime under valley breeze  
261 condition (Fu et al., 2009; Lin et al., 2019; Yin et al., 2018). The above findings at WLG suggested  
262 that local sources and in situ atmospheric transformations may only have minor impacts on PBM  
263 concentration. Instead, atmospheric circulation over the Tibetan plateau and long range transport  
264 from the other source regions should be the main factors controlling the diurnal and seasonal  
265 variations of GEM and PBM concentrations at WLG. In contrast, mean concentration of GOM  
266 during daytime ( $17.2 \pm 16.5 \text{ pg m}^{-3}$ ) was 31.3% higher than that during night ( $13.1 \pm 10.3 \text{ pg m}^{-3}$ )  
267 at WLG. Given that there was a lack of strong anthropogenic emissions around the station or in the  
268 surrounding areas, such a daytime elevated GOM phenomenon should be likely attributed to the in  
269 situ production of GOM via GEM oxidation during the daytime (Ariya et al., 2015; Fain et al., 2009).  
270 Therefore, local meteorology and photochemical production could be important controlling factors  
271 for the observed diurnal patterns of GOM at WLG.

272

### 273 **3.3 Source identification of GEM and PBM**

274 During the whole study period, the prevailing winds at WLG were from southwestern quadrant  
275 (46.5%) mainly originated from and passing over Tibetan Plateau and southern Xinjiang under the  
276 control of the westerlies. Average GEM concentrations ( $1.58$  to  $1.91 \text{ ng m}^{-3}$ ) associated with this  
277 wind sector were overall lower than those associated with other wind sectors (Fig. 4), suggesting  
278 the areas southwest of WLG were not important source regions of GEM at WLG. In contrast, GEM  
279 concentrations (means:  $2.42$  to  $2.87 \text{ ng m}^{-3}$ ) associated with northeast wind sector were highly

280 elevated. The northeast wind mainly came from the low-altitude regions in northwestern China with  
281 many anthropogenic Hg sources, which could have contributed to GEM at WLG. In contrast to  
282 GEM, maximum PBM concentrations (means: 68.6 to 97.8  $\text{pg m}^{-3}$ ) were associated with wind  
283 sectors of southwestern and northwestern quadrants and lowest PBM concentrations (means: 49.6  
284 to 63.3  $\text{pg m}^{-3}$ ) were associated with wind sector of the eastern quadrants (Fig. 4). The southwest  
285 and northwest winds were mainly originated from and passed over deserts and Gobi regions,  
286 including the largest Taklimakan Desert in Asia. These areas are the main dust source regions in  
287 middle and eastern China (Che et al., 2011; Chen et al., 2017), and therefore would be an important  
288 source of PBM at WLG.

289

290 To better understand the sources and long-range transport of atmospheric Hg at WLG, CWT  
291 values for GEM and PBM were calculated and are shown in Fig. 5. Higher GEM CWT values were  
292 mainly located in eastern Qinghai, southern Gansu, western Shanxi, and southwestern Inner  
293 Mongolia of China and northern South Asia, whereas lower values were mainly located western  
294 Qinghai, Xinjiang and Xizang provinces (Fig. 5a). By matching the gridded GEM CWT values with  
295 the gridded anthropogenic GEM emissions in the study domain, we found GEM CWT values were  
296 significantly positively correlated with anthropogenic GEM emissions ( $R^2 = 0.55, p < 0.01$ , Fig. 6a).  
297 This indicates GEM at WLG was mainly caused by long-range transport of anthropogenic GEM  
298 emissions from industrial areas in western China, and this is overall consistent with the findings  
299 discussed above that were based on wind dependence of GEM at WLG.

300

301 Differing from the case of GEM, higher PBM CWT values were mainly located in southern  
302 Xinjiang, western Qinghai and south-central Xizang provinces, whereas the regions to the east of  
303 WLG, where many industrial sources were located, showed relatively lower PBM CWT values (Fig.  
304 5b). In addition, gridded PBM CWT values showed a negative correlation with gridded  
305 anthropogenic PBM emissions (Fig. 6b). These findings indicate that long-range transport of  
306 anthropogenic PBM emission was unlikely the major sources of PBM at WLG. Instead, long-range  
307 transport of dust particles originated from deserts and Gobi regions in western China, such as  
308 Taklimakan desert, Qaidam desert and Badain Jaran desert (Fig. S5), is responsible for PBM at  
309 WLG. These regions contain the major deserts and Gobi areas in East Asia and can release up to 25  
310 million tons dust particles annually. Dusts from these regions could be transported to the  
311 northwestern, middle and even eastern China through the westerlies over the Tibetan plateau (Che  
312 et al., 2011; Chen et al., 2017; Xuan et al., 2000). Previous studies showed that atmospheric PBM  
313 concentrations ( $86.1\text{-}517 \text{ pg m}^{-3}$ ) over the Taklimakan Desert are remarkably higher than those  
314 observed from background sites in China and even comparable to those measured in most of the

315 Chinese metropolitan cities (Huang et al., 2020). We thus concluded that the dry airflows transported  
316 the PBM-enriched dust aerosols from the desert and Gobi regions to WLG, and contributed  
317 significantly to the elevated PBM concentrations at WLG.

318

### 319 **3.4 Impact of desert dust related sources on PBM**

320 To evaluate the impact of dust related sources on the temporal variations of PBM concentration,  
321 daily cumulative AAI ( $\Sigma$ AAI) encountered by air masses transported during the preceding two days  
322 were calculated, as shown in Fig. 7 together with daily PBM concentrations. PBM concentrations  
323 maintained at relatively low levels in warm months (May to September), increased since October,  
324 and reached the highest levels in winter and early spring (December to March) (Table S1). Daily  
325  $\Sigma$ AAI showed negative values from June to October, but large positive values in winter and early  
326 spring (Table S1 and Fig. 7). A significant positive correlation ( $r^2 = 0.31$ ,  $p < 0.01$ ) was observed  
327 between daily  $\Sigma$ AAI and daily PBM concentration (Fig. 7), indicating that the long-range transport  
328 of dust and/or biomass burning related sources played an important role in the temporal variations  
329 of PBM concentration at WLG. Biomass burning related sources were not likely the major causes  
330 because the air masses ended at WLG were mainly originated from and passed over regions with  
331 low biomass burning area (Fig. S5). PBM concentrations showed a negative correlation with CO  
332 and BC concentrations, which are mainly emitted from the industrial and biomass burning activities  
333 (Table S2). Hence, we conclude that the dust related sources were the dominant source of PBM at  
334 WLG. Previous studies analyzing spatiotemporal patterns of atmospheric dust based on satellite  
335 remote sensing generated dust aerosol index have shown the Taklimakan area as the dominant  
336 source of dust episodes in Asia, especially in every spring season. Desert dust is a significant carrier  
337 of atmospheric aerosol and PBM to the cryosphere of Western China and can also have global  
338 impact through long-range transport (Huang et al., 2020; Zhang et al., 2008).

339

340 Desert and Gobi areas are important sources of atmospheric particles. Global dust particle  
341 emissions were estimated to range from 500 to 5000 Tg yr<sup>-1</sup> with an average value of 1836±903 Tg  
342 yr<sup>-1</sup>. In China, the desert and Gobi dust particle emissions were estimated to range from 100 to 459  
343 Tg yr<sup>-1</sup> with an average value of 242±120 Tg yr<sup>-1</sup> (Table S3). Hg content in total suspended particles  
344 (TSP) from desert dust was averaged at 0.33 μg g<sup>-1</sup> from existing studies (Table S3). Based on the  
345 above numbers, total particulate bound mercury (Hg-TSP) emissions from desert dust related  
346 sources were roughly estimated to be 606 ± 298 (range from 165 to 1650) Mg yr<sup>-1</sup> globally and 80  
347 ± 40 (range from 33 to 151) Mg yr<sup>-1</sup> in China (Table S3). Given that PM<sub>2.5</sub> generally accounts for  
348 40% of TSP in dust aerosols, PBM (referred as to mercury bound to fine particles, e.g., of diameter  
349 <2.5 μm) emissions from desert dust related sources were 242.4 Mg yr<sup>-1</sup> globally and 32 Mg yr<sup>-1</sup> in

350 China. These values exceed the anthropogenic PBM emissions in the world (75 Mg yr<sup>-1</sup>) and China  
351 (16 Mg yr<sup>-1</sup>), suggesting desert and Gobi areas as important sources of atmospheric PBM emissions  
352 on regional to global scales.

353

354 Besides emissions from anthropogenic and dust related sources, gas-particle partitioning  
355 between GOM and PBM also affect PBM level in the atmosphere. Thus, the intrusion of GOM-rich  
356 air from free troposphere would also have an impact on PBM (Ariya et al., 2015; Lin et al., 2019;  
357 Tsamalis et al., 2014). The PBM/GEM ratios at WLG were similar to those observed at  
358 Qomolangma Natural Nature Preserve and Nam Co. in the Tibetan Plateau, but much higher than  
359 those in Chinese urban and remote areas (Lin et al., 2019; Yin et al., 2018). On the other hand, the  
360 PBM/GOM ratios at WLG were relatively lower than the values observed from the other two  
361 Tibetan sites (Fig. 8). Generally, gas-particle partitioning of GOM and PBM is mainly controlled by  
362 air temperature (Amos et al., 2012), however, no clear dependence of monthly PBM/GOM ratio on  
363 monthly mean air temperature was observed, e.g., similar PBM/GOM ratios were observed between  
364 the coldest months (December to February) and other seasons (Fig. 8). This indicates the elevated  
365 PBM in winter and early spring at WLG were not likely caused by the enhanced gas-particle  
366 partitioning of GOM under low air temperature. Besides, air masses travelling heights at WLG did  
367 not show clear seasonal variations throughout the study period, indicating elevated PBM  
368 concentrations at WLG in winter and the early spring were unlikely associated with intrusions of  
369 free troposphere air masses.

370

#### 371 **4 Conclusions**

372 This study presented the first full-year continuous speciated Hg data set and identified potential  
373 sources causing high GEM and PBM at WLG in the Tibetan Plateau. Mean GEM level at WLG was  
374 slightly higher than the background level of GEM in the Northern Hemisphere. Mean PBM level at  
375 WLG was much higher compared with the reported values in remote areas in the Northern  
376 Hemisphere. Seasonal variations in GEM concentration indicated that Hg emissions from  
377 anthropogenic source regions and long-range transport played important roles on the high GEM  
378 levels at WLG. High PBM concentrations at WLG were observed in cold season, which were mainly  
379 caused by dust aerosol sources from the desert and Gobi areas. Analysis from CWT and  $\Sigma$ AAI  
380 northern Xinjiang, eastern Qinghai, southern Gansu, southwestern Shaanxi, western Inner Mongolia  
381 of China and northern South Asia could be the main source areas of GEM, while southern Xinjiang,  
382 southwestern Inner Mongolia, northern Gansu, western Qinghai and Tibet of China were likely the  
383 source regions of PBM at WLG. Long-range transport of dust particles from desert and Gobi areas  
384 contribute to the elevated PBM at WLG. The estimated PBM emissions from dust particles

385 suggested that dust from desert and Gobi areas are critical sources of PBM on regional to global  
386 scales, which should be paid more attention in future studies.

#### 387 **Data Availability:**

388 All the dataset used in this study can be found in Supporting information.

#### 389 **Author contribution:**

390 H.Z., X.W.F, and X.B.F. initiated the project and designated the field experiments. H.Z, X.W.F.,  
391 B.Y., B.X.L., P.L., and G.P.Z. carried out the field observations. H.Z., and X.W.F. prepared the  
392 manuscript with contributions from all co-authors.

#### 393 **Acknowledgments**

394 This work is supported by the Strategic Priority Research Program (XDB40000000), Key  
395 Research Program of Frontier Sciences (ZDBS-LY-DQC029) of CAS, the National Science  
396 Foundation of China (41703134 and 41622305), and the K.C. Wong Education Foundation of CAS.  
397 We also thank staffs in Waliguan GAW Baseline Observatory for field sampling assistance.

#### 398 **Competing interests:**

399 The authors declare that they have no conflict of interest.

#### 400 **Supporting information:**

- 401 • Supporting Information Figure S1-S5
- 402 • Supporting Information Table S1-S3

403

#### 404 **Reference**

- 405 AMAP/UNEP, 2013. Geospatially Distributed Mercury Emissions Dataset 2010v1.  
406 AMAP/UNEP (2018) Technical Background Assessment for the 2018 Global Mercury Assessment.  
407 Ambrose, J.L. (2017) Improved methods for signal processing in measurements of mercury by Tekran  
408 (R) 2537A and 2537B instruments. *Atmospheric Measurement Techniques* 10, 5063-5073.  
409 Amos, H.M., Jacob, D.J., Holmes, C.D., Fisher, J.A., Wang, Q., Yantosca, R.M., Corbitt, E.S., Galarneau,  
410 E., Rutter, A.P., Gustin, M.S., Steffen, A., Schauer, J.J., Graydon, J.A., St Louis, V.L., Talbot, R.W.,  
411 Edgerton, E.S., Zhang, Y., Sunderland, E.M. (2012) Gas-particle partitioning of atmospheric Hg(II) and  
412 its effect on global mercury deposition. *Atmospheric Chemistry and Physics* 12, 591-603.  
413 Ariya, P.A., Amyot, M., Dastoor, A., Deeds, D., Feinberg, A., Kos, G., Poulain, A., Ryjkov, A., Semeniuk,  
414 K., Subir, M., Toyota, K. (2015) Mercury Physicochemical and Biogeochemical Transformation in the  
415 Atmosphere and at Atmospheric Interfaces: A Review and Future Directions. *Chemical Reviews* 115,  
416 3760-3802.  
417 Chakraborty, L.B., Qureshi, A., Vadenbo, C., Hellweg, S. (2013) Anthropogenic Mercury Flows in India  
418 and Impacts of Emission Controls. *Environmental Science & Technology* 47, 8105-8113.

419 Che, H.Z., Wang, Y.Q., Sun, J.Y. (2011) Aerosol optical properties at Mt. Waliguan Observatory, China.  
420 *Atmospheric Environment* 45, 6004-6009.

421 Chen, P.F., Kang, S.C., Li, C.L., Zhang, Q.G., Guo, J.M., Tripathee, L., Zhang, Y.A., Li, G., Gul, C.,  
422 Cong, Z.Y., Wan, X., Niu, H.W., Panday, A.K., Rupakheti, M., Ji, Z.M. (2019) Carbonaceous aerosol  
423 characteristics on the Third Pole: A primary study based on the Atmospheric Pollution and Cryospheric  
424 Change (APCC) network. *Environmental Pollution* 253, 49-60.

425 Chen, S.Y., Huang, J.P., Kang, L.T., Wang, H., Ma, X.J., He, Y.L., Yuan, T.G., Yang, B., Huang, Z.W.,  
426 Zhang, G.L. (2017) Emission, transport, and radiative effects of mineral dust from the Taklimakan and  
427 Gobi deserts: comparison of measurements and model results. *Atmospheric Chemistry and Physics* 17,  
428 2401-2421.

429 Cheng, I., Zhang, L., Blanchard, P., Dalziel, J., Tordon, R. (2013) Concentration-weighted trajectory  
430 approach to identifying potential sources of speciated atmospheric mercury at an urban coastal site in  
431 Nova Scotia, Canada. *Atmospheric Chemistry and Physics* 13, 6031-6048.

432 Cheng, I., Zhang, L.M. (2017) Uncertainty Assessment of Gaseous Oxidized Mercury Measurements  
433 Collected by Atmospheric Mercury Network. *Environmental Science & Technology* 51, 855-862.

434 Chiapello, I., Prospero, J.M., Herman, J.R., Hsu, N.C. (1999) Detection of mineral dust over the North  
435 Atlantic Ocean and Africa with the Nimbus 7 TOMS. *Journal of Geophysical Research-Atmospheres*  
436 104, 9277-9291.

437 Cole, A.S., Steffen, A., Eckley, C.S., Narayan, J., Pilote, M., Tordon, R., Graydon, J.A., St Louis, V.L.,  
438 Xu, X.H., Branfireun, B.A. (2014) A Survey of Mercury in Air and Precipitation across Canada: Patterns  
439 and Trends. *Atmosphere* 5, 635-668.

440 D'Amore, F., Bencardino, M., Cinnirella, S., Sprovieri, F., Pirrone, N. (2015) Data quality through a web-  
441 based QA/QC system: implementation for atmospheric mercury data from the global mercury  
442 observation system. *Environmental Science-Processes & Impacts* 17, 1482-1491.

443 Driscoll, C.T., Mason, R.P., Chan, H.M., Jacob, D.J., Pirrone, N. (2013) Mercury as a Global Pollutant:  
444 Sources, Pathways, and Effects. *Environmental Science & Technology* 47, 4967-4983.

445 Fain, X., Obrist, D., Hallar, A.G., Mccubbin, I., Rahn, T. (2009) High levels of reactive gaseous mercury  
446 observed at a high elevation research laboratory in the Rocky Mountains. *Atmospheric Chemistry and*  
447 *Physics* 9, 8049-8060.

448 Fu, X.W., Feng, X., Liang, P., Deliger, Zhang, H., Ji, J., Liu, P. (2012a) Temporal trend and sources of  
449 speciated atmospheric mercury at Waliguan GAW station, Northwestern China. *Atmospheric Chemistry*  
450 *and Physics* 12, 1951-1964.

451 Fu, X.W., Feng, X.B., Sommar, J., Wang, S.F. (2012b) A review of studies on atmospheric mercury in  
452 China. *Science of the Total Environment* 421, 73-81.

453 Fu, X.W., Feng, X.B., Wang, S.F., Rothenberg, S., Shang, L.H., Li, Z.G., Qiu, G.L. (2009) Temporal and  
454 spatial distributions of total gaseous mercury concentrations in ambient air in a mountainous area in  
455 southwestern China: implications for industrial and domestic mercury emissions in remote areas in China.  
456 *Science of the Total Environment* 407, 2306-2314.

457 Fu, X.W., Feng, X.B., Zhu, W.Z., Wang, S.F., Lu, J.L. (2008) Total gaseous mercury concentrations in  
458 ambient air in the eastern slope of Mt. Gongga, South-Eastern fringe of the Tibetan plateau, China.  
459 *Atmospheric Environment* 42, 970-979.

460 Fu, X.W., Maruszczak, N., Heimburger, L.E., Sauvage, B., Gheusi, F., Prestbo, E.M., Sonke, J.E. (2016)  
461 Atmospheric mercury speciation dynamics at the high-altitude Pic du Midi Observatory, southern France.  
462 *Atmospheric Chemistry and Physics* 16, 5623-5639.

463 Fu, X.W., Zhang, H., Yu, B., Wang, X., Lin, C.J., Feng, X.B. (2015) Observations of atmospheric mercury  
464 in China: a critical review. *Atmospheric Chemistry and Physics* 15, 9455-9476.

465 Giglio, L., Randerson, J.T., van der Werf, G.R. (2013) Analysis of daily, monthly, and annual burned area  
466 using the fourth-generation global fire emissions database (GFED4). *Journal of Geophysical Research-  
467 Biogeosciences* 118, 317-328.

468 Gustin, M.S., Amos, H.M., Huang, J., Miller, M.B., Heidecorn, K. (2015) Measuring and modeling  
469 mercury in the atmosphere: a critical review. *Atmospheric Chemistry and Physics* 15, 5697-5713.

470 Gustin, M.S., Dunham-Cheatham, S.M., Zhang, L. (2019) Comparison of 4 Methods for Measurement  
471 of Reactive, Gaseous Oxidized, and Particulate Bound Mercury. *Environmental Science & Technology*  
472 53, 14489-14495.

473 Herman, J.R., Bhartia, P.K., Torres, O., Hsu, C., Seftor, C., Celarier, E. (1997) Global distribution of UV-  
474 absorbing aerosols from Nimbus 7/TOMS data. *Journal of Geophysical Research-Atmospheres* 102,  
475 16911-16922.

476 Huang, J., Kang, S., Yin, R., Ram, K., Liu, X., Lu, H., Guo, J., Chen, S., Tripathee, L. (2020) Desert dust  
477 as a significant carrier of atmospheric mercury. *Environmental Pollution* 267, 115442.

478 Jonsson, S., Skjellberg, U., Nilsson, M.B., Lundberg, E., Andersson, A., Bjorn, E. (2014) Differentiated  
479 availability of geochemical mercury pools controls methylmercury levels in estuarine sediment and biota.  
480 *Nature Communications* 5.

481 Kim, P.R., Han, Y.J., Holsen, T.M., Yi, S.M. (2012) Atmospheric particulate mercury: Concentrations  
482 and size distributions. *Atmospheric Environment* 61, 94-102.

483 Kubilay, N., Oguz, T., Kocak, M., Torres, O. (2005) Ground-based assessment of Total Ozone Mapping  
484 Spectrometer (TOMS) data for dust transport over the northeastern Mediterranean. *Global  
485 Biogeochemical Cycles* 19.

486 Lan, X., Talbot, R., Castro, M., Perry, K., Luke, W. (2012) Seasonal and diurnal variations of atmospheric  
487 mercury across the US determined from AMNet monitoring data. *Atmospheric Chemistry and Physics*  
488 12, 10569-10582.

489 Lin, H.M., Tong, Y.D., Yin, X.F., Zhang, Q.G., Zhang, H., Zhang, H.R., Chen, L., Kang, S.C., Zhang, W.,  
490 Schauer, J., de Foy, B., Bu, X.G., Wang, X.J. (2019) First measurement of atmospheric mercury species  
491 in Qomolangma Natural Nature Preserve, Tibetan Plateau, and evidence of transboundary pollutant  
492 invasion. *Atmospheric Chemistry and Physics* 19, 1373-1391.

493 Lindberg, S.E., Brooks, S., Lin, C.J., Scott, K.J., Landis, M.S., Stevens, R.K., Goodsite, M., Richter, A.  
494 (2002) Dynamic oxidation of gaseous mercury in the Arctic troposphere at polar sunrise. *Environmental  
495 Science & Technology* 36, 1245-1256.

496 Loewen, M., Kang, S., Armstrong, D., Zhang, Q., Tomy, G., Wang, F. (2007) Atmospheric transport of  
497 mercury to the Tibetan plateau. *Environmental Science & Technology* 41, 7632-7638.

498 Lyman, S.N., Cheng, I., Gratz, L.E., Weiss-Penzias, P., Zhang, L.M. (2020) An updated review of  
499 atmospheric mercury. *Science of the Total Environment* 707.

500 Moulin, C., Chiapello, I. (2004) Evidence of the control of summer atmospheric transport of African dust  
501 over the Atlantic by Sahel sources from TOMS satellites (1979-2000). *Geophysical Research Letters* 31.

502 Murphy, D.M., Hudson, P.K., Thomson, D.S., Sheridan, P.J., Wilson, J.C. (2006) Observations of  
503 mercury-containing aerosols. *Environmental Science & Technology* 40, 3163-3167.

504 Obrist, D., Kirk, J.L., Zhang, L., Sunderland, E.M., Jiskra, M., Selin, N.E. (2018) A review of global  
505 environmental mercury processes in response to human and natural perturbations: Changes of emissions,  
506 climate, and land use. *Ambio* 47, 116-140.

507 Obrist, D., Moosmuller, H., Schurmann, R., Chen, L.W.A., Kreidenweis, S.M. (2008) Particulate-phase  
508 and gaseous elemental mercury emissions during biomass combustion: Controlling factors and  
509 correlation with particulate matter emissions. *Environmental Science & Technology* 42, 721-727.

510 Okamoto, S., Tanimoto, H. (2016) A review of atmospheric chemistry observations at mountain sites.  
511 *Progress in Earth and Planetary Science* 3.

512 Pirrone, N., Cinnirella, S., Feng, X., Finkelman, R.B., Friedli, H.R., Leaner, J., Mason, R., Mukherjee,  
513 A.B., Stracher, G.B., Streets, D.G., Telmer, K. (2010) Global mercury emissions to the atmosphere from  
514 anthropogenic and natural sources. *Atmospheric Chemistry and Physics* 10, 5951-5964.

515 Prospero, J.M., Ginoux, P., Torres, O., Nicholson, S.E., Gill, T.E. (2002) Environmental characterization  
516 of global sources of atmospheric soil dust identified with the Nimbus 7 Total Ozone Mapping  
517 Spectrometer (TOMS) absorbing aerosol product. *Reviews of Geophysics* 40.

518 Seigneur, C., Vijayaraghavan, K., Lohman, K., Karamchandani, P., Scott, C. (2004) Global source  
519 attribution for mercury deposition in the United States. *Environmental Science & Technology* 38, 555-  
520 569.

521 Selin, N.E. (2009) Global Biogeochemical Cycling of Mercury: A Review. *Annual Review of*  
522 *Environment and Resources* 34, 43-63.

523 Sheu, G.R., Mason, R.P. (2001) An examination of methods for the measurements of reactive gaseous  
524 mercury in the atmosphere. *Environmental Science & Technology* 35, 1209-1216.

525 Sprovieri, F., Pirrone, N., Bencardino, M., D'Amore, F., Carbone, F., Cinnirella, S., Mannarino, V., Landis,  
526 M., Ebinghaus, R., Weigelt, A., Brunke, E.G., Labuschagne, C., Martin, L., Munthe, J., Wangberg, I.,  
527 Artaxo, P., Morais, F., Barbosa, H.D.J., Brito, J., Cairns, W., Barbante, C., Dieguez, M.D., Garcia, P.E.,  
528 Dommergue, A., Angot, H., Magand, O., Skov, H., Horvat, M., Kotnik, J., Read, K.A., Neves, L.M.,  
529 Gawlik, B.M., Sena, F., Mashyanov, N., Obolkin, V., Wip, D., Bin Feng, X., Zhang, H., Fu, X.W.,  
530 Ramachandran, R., Cossa, D., Knoery, J., Maruscak, N., Nerentorp, M., Norstrom, C. (2016)  
531 Atmospheric mercury concentrations observed at ground-based monitoring sites globally distributed in  
532 the framework of the GMOS network. *Atmospheric Chemistry and Physics* 16, 11915-11935.

533 Sun, R.Y., Sun, G.Y., Kwon, S.Y., Feng, X.B., Kang, S.C., Zhang, Q.G., Huang, J., Yin, R.S. (2020)  
534 Mercury biogeochemistry over the Tibetan Plateau: An overview. *Critical Reviews in Environmental*  
535 *Science and Technology*.

536 Torres, O., Bhartia, P.K., Herman, J.R., Ahmad, Z., Gleason, J. (1998) Derivation of aerosol properties  
537 from satellite measurements of backscattered ultraviolet radiation: Theoretical basis. *Journal of*  
538 *Geophysical Research-Atmospheres* 103, 17099-17110.

539 Tsamalis, C., Ravetta, F., Gheusi, F., Delbarre, H., Augustin, P. (2014) Mixing of free-tropospheric air  
540 with the lowland boundary layer during anabatic transport to a high altitude station. *Atmospheric*  
541 *Research* 143, 425-437.

542 Wang, X., Lin, C.J., Yuan, W., Sommar, J., Zhu, W., Feng, X.B. (2016) Emission-dominated gas  
543 exchange of elemental mercury vapor over natural surfaces in China. *Atmospheric Chemistry and*  
544 *Physics* 16, 11125-11143.

545 Wang, Y.Q., Zhang, X.Y., Draxler, R.R. (2009) TrajStat: GIS-based software that uses various trajectory  
546 statistical analysis methods to identify potential sources from long-term air pollution measurement data.  
547 *Environmental Modelling & Software* 24, 938-939.

548 Wright, L.P., Zhang, L.M., Cheng, I., Aherne, J., Wentworth, G.R. (2018) Impacts and Effects Indicators  
549 of Atmospheric Deposition of Major Pollutants to Various Ecosystems - A Review. *Aerosol and Air*  
550 *Quality Research* 18, 1953-1992.

551 Wu, Y., Wang, S.X., Streets, D.G., Hao, J.M., Chan, M., Jiang, J.K. (2006) Trends in anthropogenic  
552 mercury emissions in China from 1995 to 2003. *Environmental Science & Technology* 40, 5312-5318.  
553 Xu, W.Y., Xu, X.B., Lin, M.Y., Lin, W.L., Tarasick, D., Tang, J., Ma, J.Z., Zheng, X.D. (2018) Long-  
554 term trends of surface ozone and its influencing factors at the Mt Waliguan GAW station, China - Part 2:  
555 The roles of anthropogenic emissions and climate variability. *Atmospheric Chemistry and Physics* 18,  
556 773-798.  
557 Xuan, J., Liu, G.L., Du, K. (2000) Dust emission inventory in Northern China. *Atmospheric Environment*  
558 34, 4565-4570.  
559 Yin, X.F., Kang, S.C., de Foy, B., Ma, Y.M., Tong, Y.D., Zhang, W., Wang, X.J., Zhang, G.S., Zhang,  
560 Q.G. (2018) Multi-year monitoring of atmospheric total gaseous mercury at a remote high-altitude site  
561 (Nam Co, 4730 m a.s.l.) in the inland Tibetan Plateau region. *Atmospheric Chemistry and Physics* 18,  
562 10557-10574.  
563 Zhang, B., Tsunekawa, A., Tsubo, M. (2008) Contributions of sandy lands and stony deserts to long-  
564 distance dust emission in China and Mongolia during 2000-2006. *Global and Planetary Change* 60, 487-  
565 504.  
566 Zhang, H., Fu, X.W., Lin, C.J., Shang, L.H., Zhang, Y.P., Feng, X.B., Lin, C. (2016) Monsoon-facilitated  
567 characteristics and transport of atmospheric mercury at a high-altitude background site in southwestern  
568 China. *Atmospheric Chemistry and Physics* 16, 13131-13148.  
569 Zhang, H., Fu, X.W., Lin, C.J., Wang, X., Feng, X.B. (2015a) Observation and analysis of speciated  
570 atmospheric mercury in Shangri-La, Tibetan Plateau, China. *Atmospheric Chemistry and Physics* 15,  
571 653-665.  
572 Zhang, H., Fu, X.W., Wang, X., Feng, X.B. (2019) Measurements and Distribution of Atmospheric  
573 Particulate-Bound Mercury: A Review. *Bulletin of Environmental Contamination and Toxicology* 103,  
574 48-54.  
575 Zhang, L., Wang, S.X., Wang, L., Wu, Y., Duan, L., Wu, Q.R., Wang, F.Y., Yang, M., Yang, H., Hao, J.M.,  
576 Liu, X. (2015b) Updated Emission Inventories for Speciated Atmospheric Mercury from Anthropogenic  
577 Sources in China. *Environmental Science & Technology* 49, 3185-3194.  
578 Zhao, Z.Z., Cao, J.J., Shen, Z.X., Xu, B.Q., Zhu, C.S., Chen, L.W.A., Su, X.L., Liu, S.X., Han, Y.M.,  
579 Wang, G.H., Ho, K.F. (2013) Aerosol particles at a high-altitude site on the Southeast Tibetan Plateau,  
580 China: Implications for pollution transport from South Asia. *Journal of Geophysical Research-*  
581 *Atmospheres* 118, 11360-11375.  
582  
583  
584  
585  
586  
587  
588  
589  
590

591 **Figure Captions**

592 **Fig. 1:** The map showing the location of WLG, and distributions of the deserts and cities around  
593 WLG.

594 **Fig. 2:** Time series of hourly GEM, GOM and PBM concentrations in ambient air at WLG.

595 **Fig. 3:** Monthly means of GEM, GOM and PBM at WLG during a full-year sampling period. Error  
596 bars indicate the 1sd of monthly mean values.

597 **Fig. 4:** Frequency distribution of wind direction and wind-sector based mean GEM and PBM  
598 concentrations during the study period.

599 **Fig. 5:** Identified source regions of atmospheric GEM and PBM at WLG during the study period.  
600 (A) gridded ( $0.5^\circ \times 0.5^\circ$ ) values for GEM, and (B) gridded ( $0.5^\circ \times 0.5^\circ$ ) values for PBM. Gray line  
601 enclosed regions indicate desert locations in China.

602 **Fig. 6:** Correlation between the simulated GEM or PBM CWT value and their respective  
603 anthropogenic emissions (AMAP/UNEP, 2018). The location of each gridded CWT value is  
604 matched with that of anthropogenic emission. Gridded anthropogenic emissions are divided into 20  
605 groups with equal number of grids, starting from the lowest to highest emission values.

606 **Fig. 7:** Variations in daily mean PBM concentration and daily cumulative Absorbing Aerosol Index  
607 (AAI) during the proceeding two days at WLG.

608 **Fig. 8:** The monthly PBM/GEM and PBM/GOM ratio with air temperature and air mass traveling  
609 height during a full-year sampling period. Column (a) is the mean PBM/GEM and PBM/GOM ratios  
610 at Qomolangma Natural Nature Preserve and Nam Co in the inland Tibetan Plateau, column (b) is  
611 the mean PBM/GEM and PBM/GOM ratios of Chinese cities, and column (c) is the mean  
612 PBM/GEM and PBM/GOM ratios of Chinese remote areas.

613

614

615

616

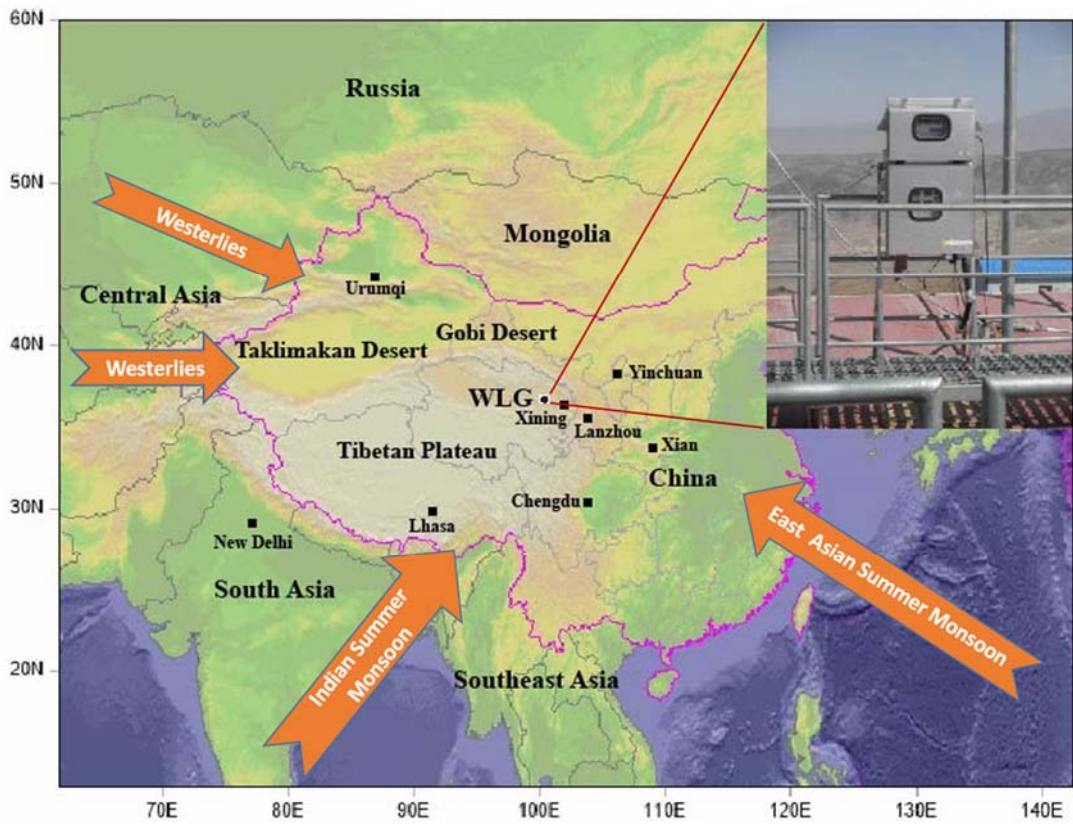
617

618

619

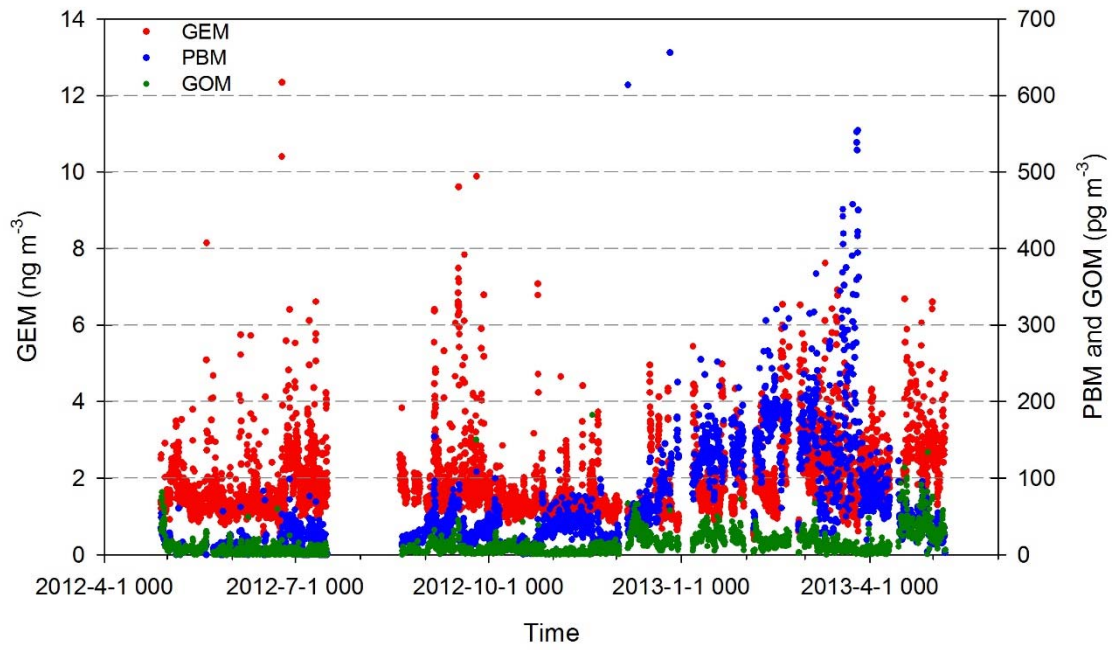
620

621 **Fig. 1:** The map showing the location of WLG, and distributions of the deserts and cities around  
622 WLG.



623  
624  
625

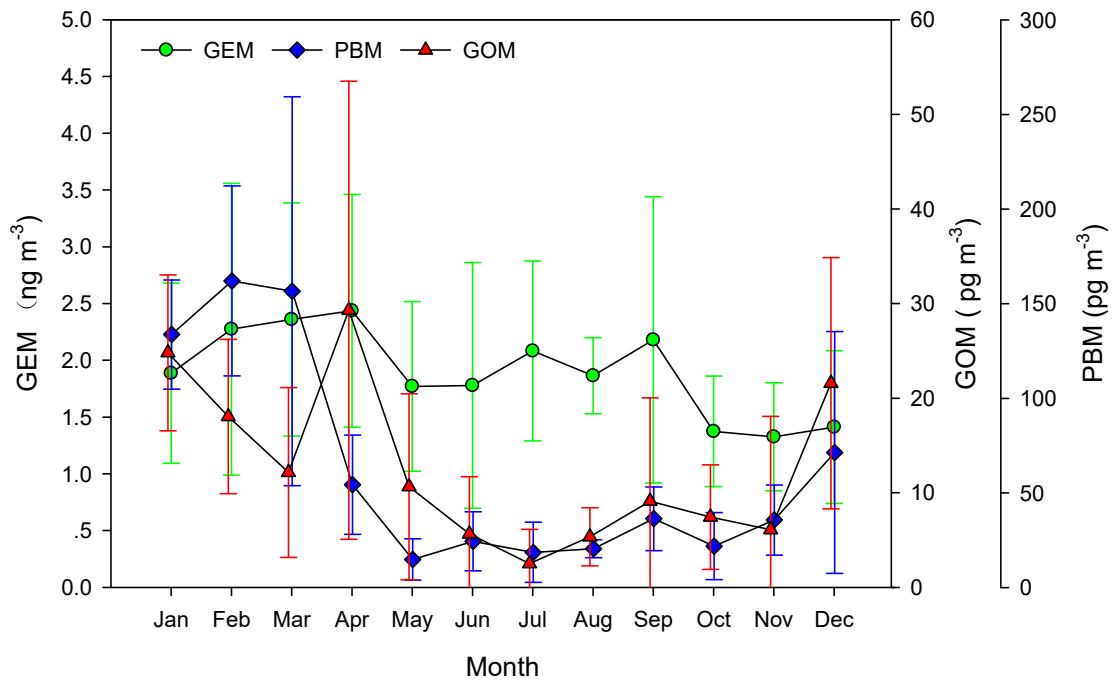
626 **Fig. 2:** Time series of hourly GEM, GOM and PBM concentrations in ambient air at WLG.



627

628

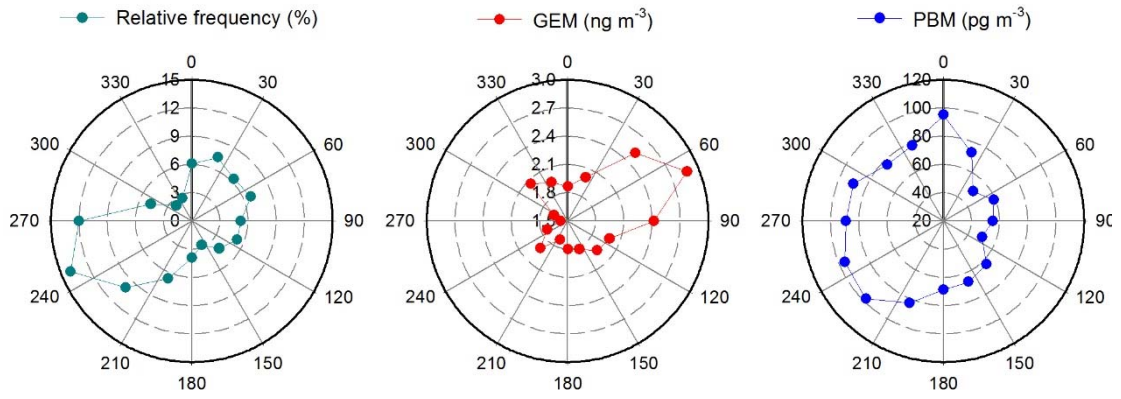
629 **Fig. 3:** Monthly means of GEM, GOM and PBM at WLG during a full-year sampling period. Error  
630 bars indicate the 1sd of monthly mean values.



631

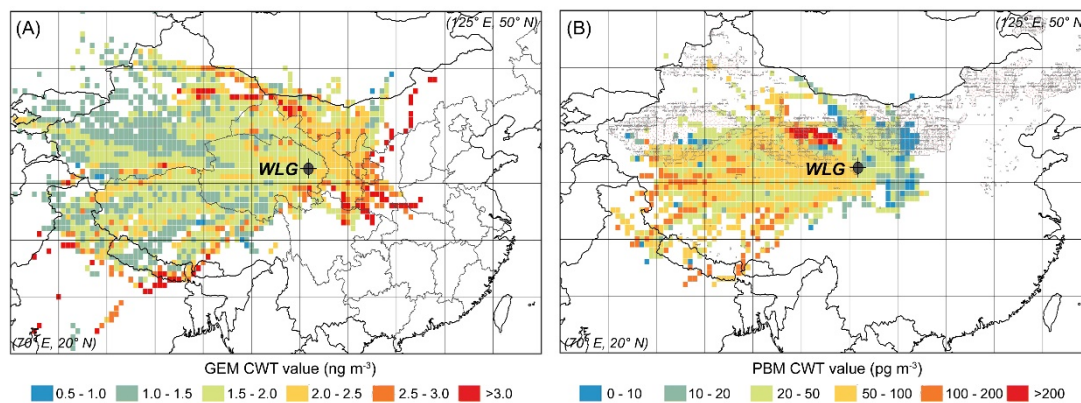
632

633 **Fig. 4:** Frequency distribution of wind direction and wind-sector based mean GEM and PBM  
634 concentrations during the study period.



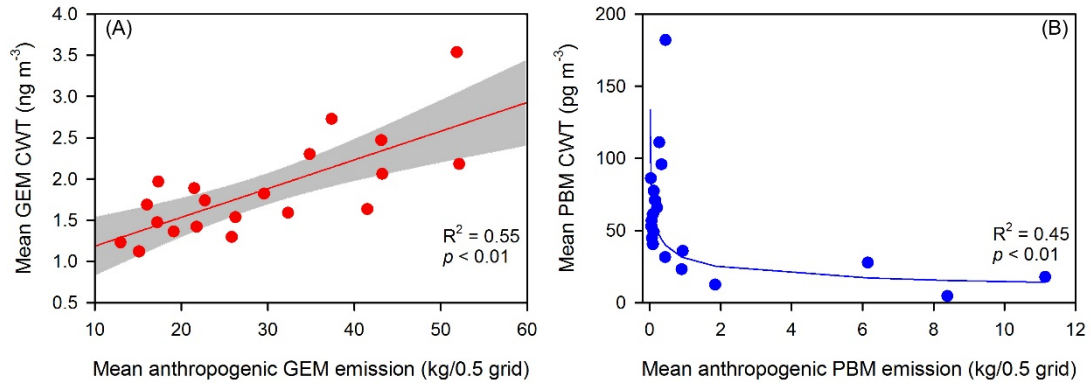
635  
636  
637

638 **Fig. 5:** Identified source regions of atmospheric GEM and PBM at WLG during the study period.  
639 (A) gridded ( $0.5^\circ \times 0.5^\circ$ ) CWT values for GEM, and (B) gridded ( $0.5^\circ \times 0.5^\circ$ ) CWT values for PBM.  
640 Gray line enclosed regions indicate desert locations in China.



641  
642  
643

644 **Fig. 6:** Correlation between the simulated GEM or PBM CWT value and their respective  
645 anthropogenic emissions (AMAP/UNEP, 2018). The location of each gridded CWT value is  
646 matched with that of anthropogenic emission. Gridded anthropogenic emissions are divided into 20  
647 groups with equal number of grids, starting from the lowest to highest emission values.  
648

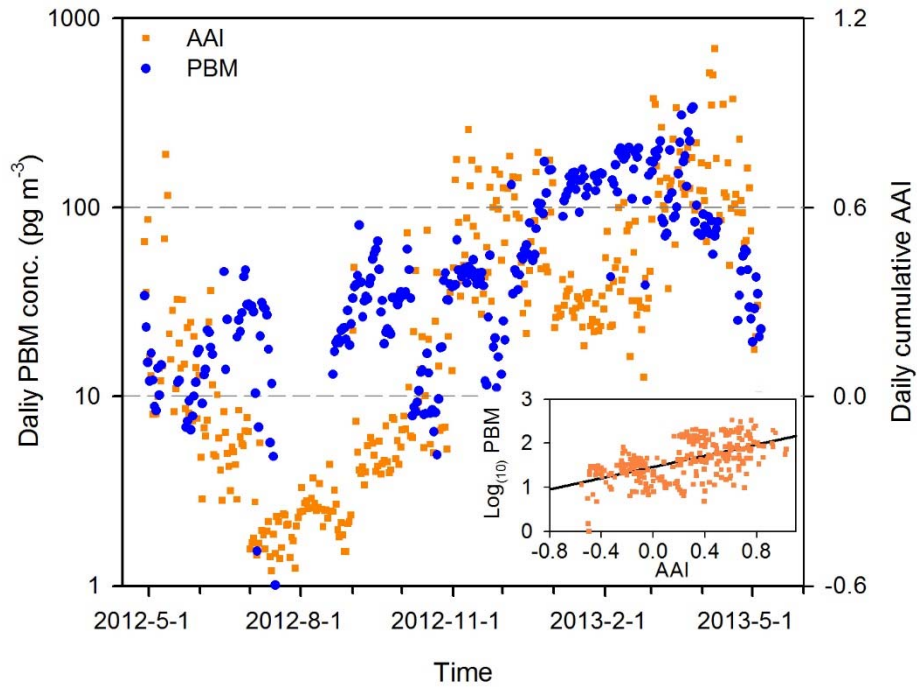


649

650

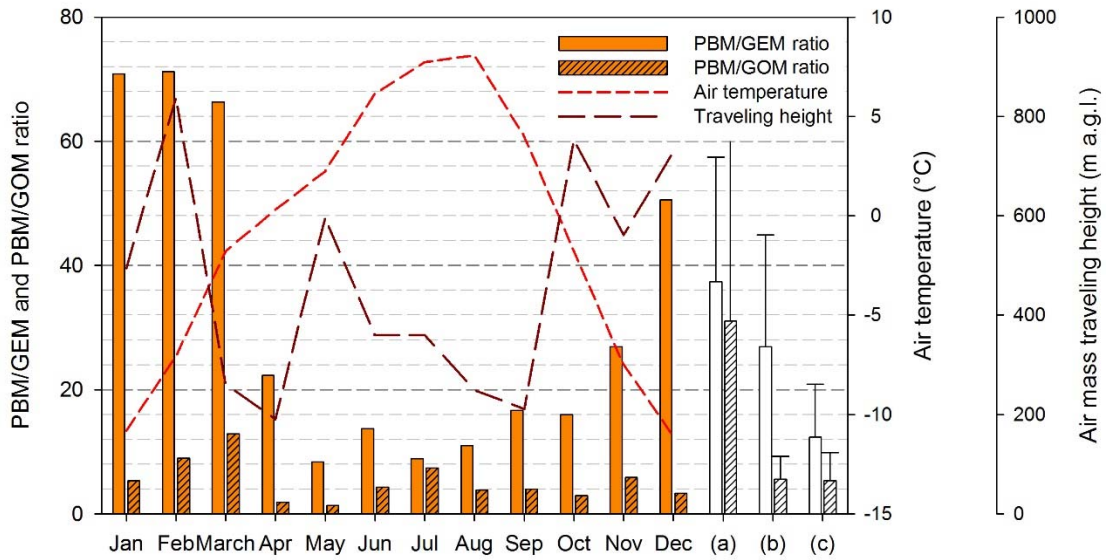
651

652 **Fig. 7:** Variations in daily mean PBM concentration and daily cumulative Absorbing Aerosol Index  
653 (AAI) during the preceding two days at WLG.



654  
655  
656  
657

658 **Fig. 8:** The monthly PBM/GEM and PBM/GOM ratio with air temperature and air mass traveling  
 659 height during a full-year sampling period. Column (a) is the mean PBM/GEM and PBM/GOM ratios  
 660 at Qomolangma Natural Nature Preserve and Nam Co in the inland Tibetan Plateau, column (b) is  
 661 the mean PBM/GEM and PBM/GOM ratios of Chinese cities, and column (c) is the mean  
 662 PBM/GEM and PBM/GOM ratios of Chinese remote areas.



663

664

665